

LOW-ENERGY BEHAVIOR OF THE $^3\text{He}(\alpha, \gamma)^7\text{Be}$ CROSS SECTION

J. L. OSBORNE[†], C. A. BARNES, R. W. KAVANAGH, R. M. KREMER, G. J. MATHEWS^{††}
and J. L. ZYSKIND^{†††}

W. K. Kellogg Radiation Laboratory, California Institute of Technology, Pasadena, California 91125, USA

P. D. PARKER

*A. W. Wright Nuclear Structure Laboratory, Yale University, New Haven, Connecticut 06520
and*

W. K. Kellogg Laboratory, California Institute of Technology, Pasadena, California 91125, USA

and

A. J. HOWARD

Trinity College, Hartford, Connecticut 06106

and

W. K. Kellogg Radiation Laboratory, California Institute of Technology, Pasadena, California 91125, USA

Received 27 September 1983

Abstract: Cross sections for the $^3\text{He}(\alpha, \gamma)^7\text{Be}$ reaction have been measured at several energies from $E_{\text{c.m.}} = 165$ to 1169 keV by counting prompt γ -rays from a windowless, differentially pumped, recirculating, ^3He gas target. The cross-section factor $S_{34}(E_{\text{c.m.}})$ and branching ratio γ_1/γ_0 were determined at each energy. Cross sections were also measured at $E_{\text{c.m.}} = 947$ and 1255 keV by counting the γ -rays from the ^7Be produced in a ^3He gas cell with a Ni entrance foil. Combining the results of these two independent experiments yields a zero-energy intercept for the cross-section factor of $S_{34}(0) = 0.53 \pm 0.03$ keV·b. The relationship between these measurements and several theoretical calculations, and the import of the extrapolated cross section for the solar-neutrino problem are discussed.

E

NUCLEAR REACTIONS $^3\text{He}(\alpha, \gamma)$, $E = 165$ to 1169 keV; measured $\sigma(E)$, E_γ , branching ratio, $^3\text{He}(\alpha, \gamma)$, $E(\text{cm}) = 947, 1255$ keV; measured $\sigma(E)$. Enriched target.

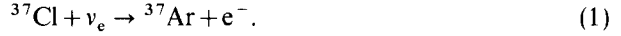
[†] Present address: Nuclear Physics Laboratory, University of Washington, Seattle, Washington 98195, USA.

^{††} Present address: University of California, Lawrence Livermore National Laboratory, Livermore, California 94550, USA.

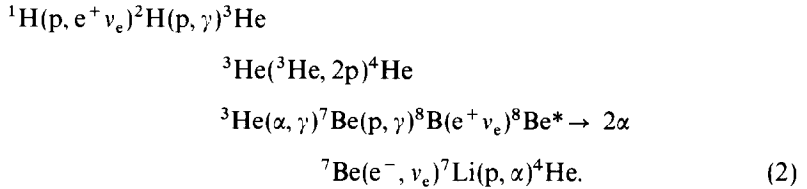
^{†††} Present address: Bell Telephone Laboratories, Holmdel, New Jersey 07733, USA.

1. Introduction

Since 1968, the Brookhaven solar-neutrino experiment ¹⁾ has been measuring the solar-neutrino flux using the endoergic neutrino-capture reaction



The observed rate ²⁾ for this reaction is 1.8 ± 0.3 SNU (1 SNU = 10^{-36} captures per ${}^{37}\text{Cl}$ atom per second), while the most recent solar-model calculations ³⁾ yield a theoretical capture rate of 7.6 ± 1.1 SNU. This discrepancy has become known as the solar-neutrino problem. Most of the suggestions that have been offered to resolve this problem fit into three categories: modifications to the structure or evolution of solar models, changes in the underlying particle physics, and uncertainties in the measured cross sections for the competing ${}^3\text{He}$ -burning and ${}^7\text{Be}$ -burning nuclear reactions in the proton-proton chain,



Since the energetic neutrinos from the decay of the ${}^8\text{B}$ are predicted by the calculations to be responsible for about 80% of the neutrino captures in a ${}^{37}\text{Cl}$ detector ³⁾, the reactions that lead to the production of ${}^8\text{B}$ are particularly important.

The continuing solar-neutrino problem prompted an experimental group at Münster ⁴⁾ to undertake a remeasurement of the low-energy ${}^3\text{He}(\alpha, \gamma){}^7\text{Be}$ cross section. Substantial disagreement between their results and the earlier measurements of Parker and Kavanagh ⁵⁾ and Nagatani *et al.* ⁶⁾ have motivated us to carry out an additional remeasurement of the cross section for this reaction ⁷⁾.

2. Experimental apparatus and procedure

Because the cross section for ${}^3\text{He}(\alpha, \gamma){}^7\text{Be}$ is too small to be measured directly at the energies relevant to the solar interior ($E_{\text{c.m.}} \approx 20$ keV; $\sigma \approx 3 \times 10^{-18}$ b), there are two essential aspects to these cross-section measurements: (i) an accurate determination of the absolute magnitude of the cross section at laboratory energies, and (ii) an accurate determination of the energy dependence of the cross section so that it can be reliably extrapolated to solar energies. Our experiments have

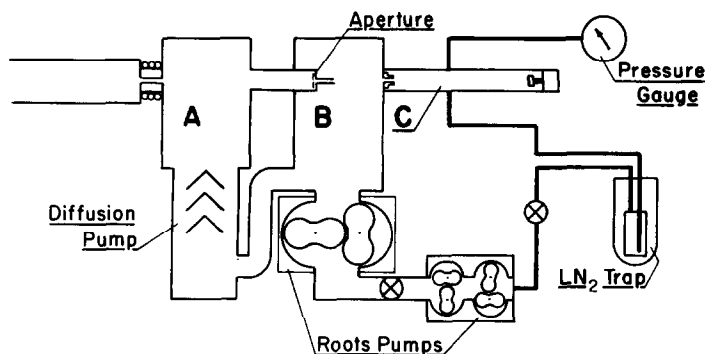


Fig. 1. Schematic representation of the gas pumping, recirculating, and purifying system for the windowless target. The canals, chambers, and apertures are described in detail in subsect. 2.1.

included (subsect. 2.1) cross-section measurements using a differentially pumped gas target over the range $165 \text{ keV} < E_{\text{c.m.}} < 1169 \text{ keV}$ in order to determine both the absolute magnitude and the energy dependence of the ${}^3\text{He}(\alpha, \gamma){}^7\text{Be}$ reaction cross section as well as (subsect. 2.2) independent total cross-section measurements of the ${}^7\text{Be}$ activity produced in an enclosed gas cell at $E_{\text{c.m.}} = 947 \text{ keV}$ and $E_{\text{c.m.}} = 1255 \text{ keV}$.

2.1. DIFFERENTIALLY PUMPED GAS-TARGET MEASUREMENTS

The differentially pumped, windowless, recirculating gas-target system is shown schematically in fig. 1 and has been described previously by Dwarakanath and Winkler⁸). The system consists of three chambers separated from one another, and from the beam line, by a series of canals. The target chamber (C) is 29 cm long from the upstream end of its entrance canal to the face of the beamstop (fig. 2). Gas pressure in the target cell is monitored with a model FA-160 Wallace and Tiernan pressure gauge, which reads 20 Torr full scale. This gauge was calibrated to 2% accuracy against a compound mercury manometer. The entrance canal between chamber (B) and the gas target is a 3.2 cm long tantalum tube; the first 6 mm has a diameter of 4.3 mm, the remaining 2.6 cm has a diameter of 4.6 mm. Chamber (B) is pumped by a Heraeus model 1600 Roots pump. The output of this pump is compressed by a Heraeus model 152 two-stage Roots pump and fed through a heat exchanger and a liquid-nitrogen-cooled zeolite trap (for gas purification) back to the gas target. Chamber (A) is separated from chamber (B) by a 10 cm long stainless-steel canal 5.4 mm in diameter and from the beam line by a 7.5 cm long, 9.7 mm diameter water-cooled canal. On the upstream side of the canal between (A) and (B) there is an electrically isolated 3.2 mm diameter tantalum aperture; the first 5 cm of this canal contains a tantalum sleeve with an

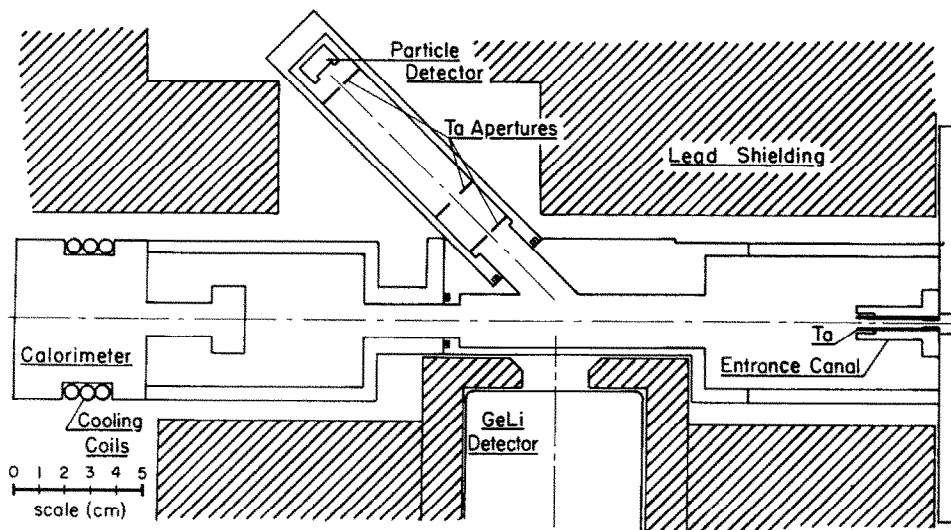


Fig. 2. The windowless gas target, (C) in fig. 1, from the entrance canal to the calorimeter. The target chamber and the Ge(Li) detector were surrounded with 10 cm of Pb shielding to reduce γ -ray background.

inside diameter of 4.6 mm. Chamber (A) is pumped directly by an oil diffusion pump, and the outlet of this pump is connected back to chamber (B). With this differentially pumped system we were able to operate with typical 99.9% enriched ^3He target pressures of 2–3 Torr with a beam-line vacuum of less than 4×10^{-6} Torr.

The front face of the γ -ray detector (100 cm^3 Ge(Li)) was 25 mm from the beam axis oriented at 90° with respect to the beam path. A 25 mm diameter aperture in a 12 mm thick lead sheet was located between the detector and the target chamber in order to limit the acceptance angles of the detector. This reduced the broadening of the γ -ray lines (due to Doppler shift and beam-energy loss in the target) and also shielded against background radiation from the entrance canal and the beamstop. The γ -ray detector efficiency was measured, as a function of γ -ray energy and as a function of position in the target chamber, by moving calibrated ^{56}Co , ^{152}Eu , and ^7Be sources along the axis of the target chamber, accumulating spectra at 1 cm intervals. In order to reduce γ -ray background, the entire target chamber and the Ge(Li) detector were surrounded by 10 cm of lead shielding. A ruggedized silicon surface-barrier particle detector was located at an angle of 45° . The solid angle of this detector was defined by two 0.125 mm thick tantalum apertures, a 1.0 mm vertical slit at 4.7 cm and a 0.62 mm circular hole at 12.7 cm from the center of the beam path. The particle-detector was used to monitor contaminant gases and to check beam current and target pressure. Typical particle spectra are shown in fig. 3.

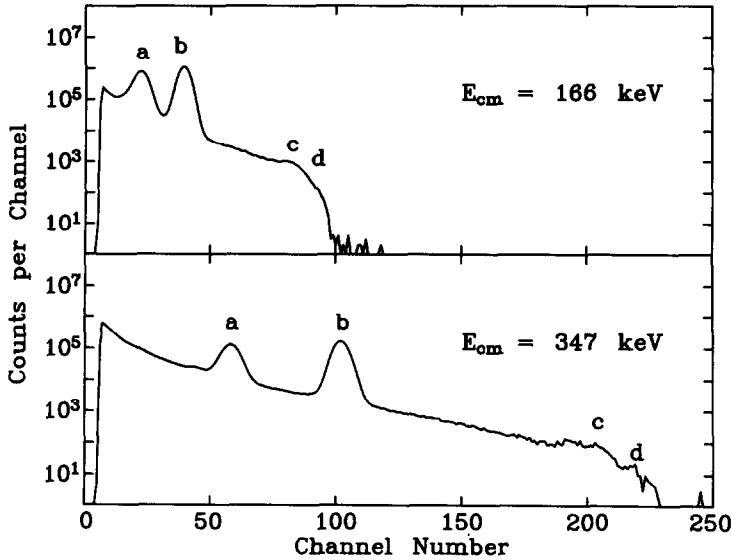


Fig. 3. Typical particle-detector spectra measured at $E_{c.m.} = 166$ and 347 keV. The 166 keV spectrum represents 0.31 particle-C of beam, while the 347 keV spectrum was acquired for 0.29 particle-C. The indicated peak positions are: (a) scattered ${}^4\text{He}$; (b) recoil ${}^3\text{He}$; (c) ${}^4\text{He}$ scattered from ${}^{14}\text{N}$; (d) ${}^4\text{He}$ scattered from ${}^{40}\text{Ar}$.

At low energies ($E_\alpha < 1200$ keV), 20 to $60 \mu\text{A}$ ${}^4\text{He}^+$ ion beams from the ONR-Caltech Model-JN Electrostatic Accelerator were used. The beams were energy-analyzed with a 30° bending magnet whose magnetic field strength was monitored with a temperature stabilized Hall probe, calibrated prior to each run with the 401 and 819 keV resonances in the ${}^7\text{Li}(\alpha, \gamma)$ reaction. The energy resolution of this system was $\pm 0.3\%$. Using the ONR-Caltech Model-EN tandem accelerator and a 90° analyzing magnet with energy resolution better than $\pm 0.1\%$, two additional measurements were made at $E_\alpha = 1200$ and 2740 keV. Since the ${}^3\text{He}(\alpha, \gamma){}^7\text{Be}$ reaction is a direct-capture, non-resonant reaction, the beam energy can also be determined from a measurement of the energy of the primary γ -rays,

$$E_{c.m.} = E_\gamma - Q. \quad (3)$$

Recoil corrections to E_γ were not made; their effect on extracted cross sections ranges from 0.8% at the lowest bombarding energy to 0.07% at the highest. Comparisons between the beam energies determined in this manner and those determined from the Hall-probe calibration always showed agreement to better than ± 1.9 keV. Beam energies were chosen to be at minima in the ${}^{13}\text{C}(\alpha, n)$ reaction yield to reduce possible neutron-induced background.

Conventional current integration is not practical with differentially pumped gas

targets because of ionization and charge exchange in the gas target. We therefore measured and integrated the beam intensity using a single-cup calorimeter⁹⁾ designed for this measurement. This device integrates the beam power by sensing the temperature difference between temperature transducers at the ends of a copper conduction rod connecting the beamstop to a constant-temperature heat sink. With no gas in the target, comparison with electrical integration showed this device to be accurate to $\pm 1\%$ over a range of beam power from 1 to 30 W.

The low-energy measurements were made in groups of 2 to 4 different energies, under identical detector and calorimeter conditions, with one measurement in each group at $E_{\text{c.m.}} = 340$ keV ($E_{\text{lab}} = 819$ keV); this provided a very accurate relative normalization of these data for determining the energy dependence of these cross sections. Target pressure, calorimeter base temperature, analyzing-magnet current, Hall-probe reading, beam current and integrated charge were recorded at least once every hour. Every two hours, the accumulated γ -ray and particle spectra were written on magnetic tape, and a new particle spectrum was started. Before and after each group of measurements, the Hall probe in the 30° analyzing magnet was calibrated using the $^7\text{Li}(\alpha, \gamma)$ resonances, and γ -ray spectra of ^{152}Eu and ^{56}Co sources were measured as an energy calibration of the Ge(Li) detector. At low energies, where the counting periods were longer, the natural background lines from ^{40}K and ^{228}Th provided a simultaneous check of detector calibration.

2.2. GAS-CELL ACTIVITY MEASUREMENTS

The gas target for the activation measurements is shown in fig. 4. The beam was collimated by a pair of 2 mm diameter tantalum apertures. Two 4 mm diameter copper tubes provided increased pumping to the volume downstream from the apertures. An aluminum electron-suppression ring (-300 V) was connected between the beam line and the target cell by 2.5 cm sections of ceramic insulator. Current flow to the suppressor was monitored, and was always less than 1% of the total beam current on target. The beam entered the target cell through a window

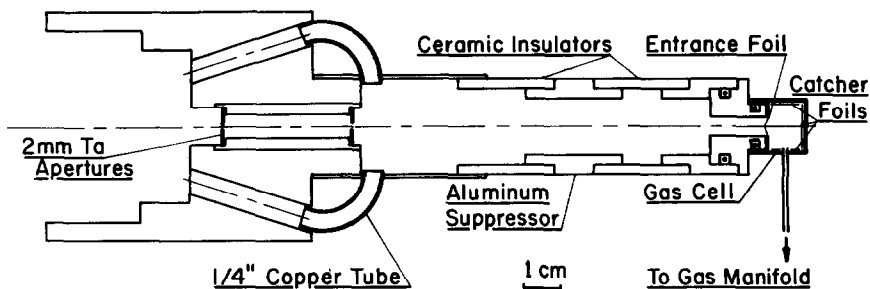


Fig. 4. The gas-cell target used in the activity measurements.

consisting of a $0.66\ \mu\text{m}$ nickel foil on which $0.20\ \mu\text{m}$ of copper had been deposited in order to increase its thermal conductivity, allowing the use of a higher beam current. The entrance foil was attached to the foil holders with high-vacuum epoxy. The target cell was made of $0.4\ \text{mm}$ thick stainless steel with an inside diameter of $12.7\ \text{mm}$. The length of the target cell was approximately $10\ \text{mm}$. A $0.025\ \text{mm}$ platinum catcher foil was indium-soldered to the end of the target cell, and the sides of the cell were also lined with platinum foil. The cell was connected to a gas manifold by a $2\ \text{mm}$ diameter stainless steel tube with a section of glass insulator. The beam current was integrated in the conventional manner by collecting the current from the electrically isolated target.

Beams of ${}^4\text{He}^+$ ions from the ONR-Caltech Model-EN tandem accelerator were used for the two activation measurements at $E_\alpha = 2.75$ and $3.40\ \text{MeV}$. The beams were analyzed with a 90° magnet stabilized by a digital NMR gaussmeter. Beam current was kept below $0.55\ \mu\text{A}$ to protect the entrance foil and to limit target heating. During the runs, the end of the target cell was cooled by a stream of air. Beam current, total accumulated charge, NMR frequency and target pressure (typically $370\ \text{Torr}$ of 99.9% ${}^3\text{He}$ gas) were recorded at least once every hour. Gas was added when the pressure fell by more than 1% . The production was continued until the estimated number of ${}^7\text{Be}$ atoms produced exceeded 4×10^6 .

The length of the target cell was measured with a depth micrometer. Additional target length (typically $0.25\ \text{mm}$) from bowing of the entrance foil caused by gas pressure was measured relative to the foil holder by using a calibrated traveling microscope. The platinum catcher foil was then removed from the target cell and attached to a $3\ \text{mm}$ thick lucite source holder on the front face of the Ge(Li) detector. The beam spot on the platinum catcher foil was aligned with a fiducial mark on the source holder so that it would be centered on the detector. The γ -ray detection efficiency was measured by counting a weak ${}^7\text{Be}$ source in this same geometry. The γ -ray strength of this source was calibrated using a $7.6 \times 7.6\ \text{cm}$ NaI(Tl) detector whose full-energy peak efficiency at $E_\gamma = 511\ \text{keV}$ was measured by counting annihilation radiation in coincidence with γ -rays from the decay of ${}^{22}\text{Na}$. During the ${}^7\text{Be}$ counting, the detector was surrounded by $10\ \text{cm}$ of lead to reduce background. The side and entrance foils were also counted in this manner to determine if any of the implanted ${}^7\text{Be}$ had been sputtered out of the foil by the beam. In both of the measurements, the inferred ${}^7\text{Be}$ content in the side and entrance foils was less than 1% of the amount in the catcher foil.

The beam energy in these activation runs was measured in two ways: (i) by measuring the energy of the direct-capture γ -rays, and (ii) by using the energy calibration of the 90° magnet together with measurements of the energy losses in the Ni+Cu entrance foil and the ${}^3\text{He}$ gas. Prompt γ -rays from the target cell were monitored with a $7.6 \times 7.6\ \text{cm}$ NaI(Tl) scintillator, with the front face of the detector $2\ \text{cm}$ from the center of the target cell, and oriented at 90° to the beam in order to eliminate the average Doppler shift. The beam energy loss in the entrance

foil was measured by observing the energy shift in narrow (α, γ) resonances with the beam passing through the foil. For the measurement at $E_\alpha = 3400$ keV, the 3189 keV resonance in ${}^{24}\text{Mg}(\alpha, \gamma)$ was used. A metallic magnesium target was prepared by reducing and evaporating 99.94% enriched ${}^{24}\text{MgO}$ onto a 0.25 mm, oxygen-free copper blank. This target was then indium-soldered to the end of the gas cell. The 11.0 and 12.7 MeV γ -rays from this reaction were counted using a 7.6×7.6 cm Na(Tl) scintillator; excitation functions for the resonance were produced, first with no entrance foil, and then with the entrance foil plus 95, 190, and 380 Torr of ${}^3\text{He}$ gas in the cell. For the measurement at $E_\alpha = 2750$ keV a resonance in ${}^{14}\text{N}(\alpha, \gamma)$ at $E_\alpha = 2348$ keV was used. Reaction γ -rays between 2.8 and 6.5 MeV were counted for target gas pressures of 160 and 340 Torr. Comparisons between the beam-energy measurements based on the measured γ -ray energies and those based on the energy-loss measurements agreed to within 4 keV.

The effect of beam heating in the target was also studied by using the ${}^{24}\text{Mg}(\alpha, \gamma)$ resonance. At a ${}^3\text{He}$ target pressure of 380 Torr, the shift in beam energy at resonance was measured with 150, 300, and 450 nA of beam current. It was found that the 450 nA beam produced a 6% decrease in effective target thickness, more than the 3% predicted on the basis of energy loss in the gas. It is believed that at least some of the additional 3% decrease is caused by local heating of the gas in the region of the entrance foil.

3. Data analysis

3.1. DIFFERENTIALLY PUMPED GAS-TARGET MEASUREMENTS

Typically γ -ray spectra for $E_{\text{c.m.}} = 166, 347$, and 507 keV are shown in fig. 5. The capture γ -ray peaks (γ_0 , γ_1 and γ_{429} in fig. 6) and the important background γ -ray yield (Y_i) and the statistical error (ΔY_i) for each transition were calculated by integrating the total number of counts under the peak and subtracting the number of counts below a linear least-squares fit to background regions above and below the peak. The effective beam energy at the center of the target was calculated from the centroid of the γ_0 peak using eq. (3).

The relationship between the extracted yields, Y_i , and the capture cross sections, $\sigma_i(E_{\text{c.m.}})$, is complicated by the use of an extended target in which both the cross section and the detector efficiency are functions of position (x) along the target axis. Therefore, the observed yield must be expressed as an integral over the length of the target,

$$Y_i = \int \sigma_i(E_{\text{c.m.}}) f_i(E_{\text{c.m.}}, \vartheta) N_\alpha n_t \varepsilon(E_{\gamma_i}, x) dx, \quad (4)$$

where Y_i is the total yield of γ_i from the extended target, $f_i(E_{\text{c.m.}}, \vartheta)$ is the angular distribution function of γ_i , N_α the total number of beam particles, n_t the target

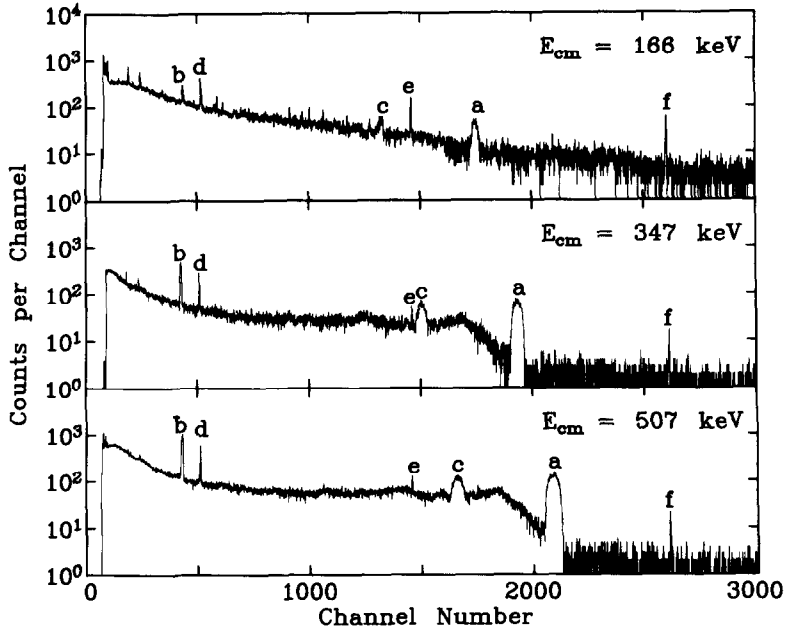


Fig. 5. Spectra of the direct-capture γ -rays for the $E_{\text{c.m.}} = 166$ keV run, the 347 keV run and the 507 keV run. The indicated γ -ray transitions are: (a) γ_0 , direct capture to the ground state of ${}^7\text{Be}$; (b) γ_{429} , first excited state to ground-state transition in ${}^7\text{Be}$; (c) γ_1 , direct capture to the first excited state of ${}^7\text{Be}$; (d) 511 keV, annihilation; (e) 1460 keV, ${}^{40}\text{K}$ decay background; (f) 2614 keV, ${}^{232}\text{Th}$ decay-chain background.

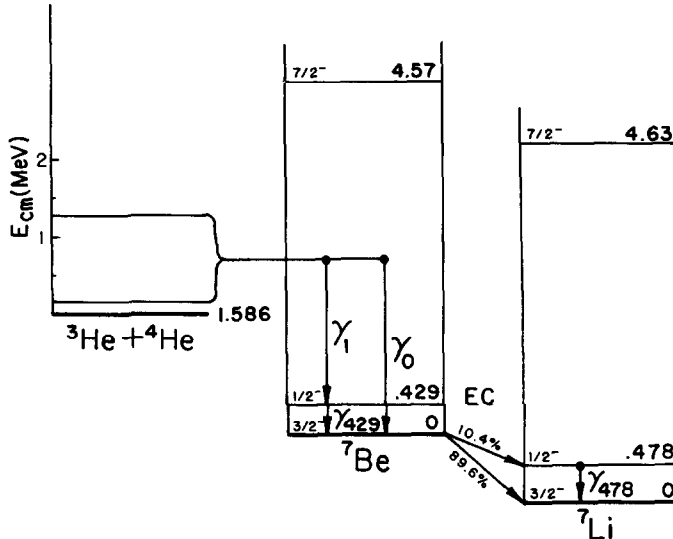


Fig. 6. The energy-level diagram for the ${}^3\text{He}(\alpha, \gamma){}^7\text{Be}$ reaction and for the subsequent decay of the ${}^7\text{Be}$. The γ -rays (γ_0 , γ_1 , γ_{429} , and γ_{478}) referred to in the text are shown.

number density, and $\varepsilon(E_\gamma, x)$ the detection efficiency as a function of γ -ray energy and position.

Substituting the expression for σ_i in terms of the cross-section factor (S) into eq. (4), and assuming that the cross-section factor is constant over the range of energies in the target, gives

$$Y_i = S_i N_x n_t \int \frac{1}{E_{\text{c.m.}}} \exp \left[\frac{-164.125}{E_{\text{c.m.}}(\text{keV})} \right] f_i(E_{\text{c.m.}}, \vartheta) \varepsilon(E_\gamma, x) dx. \quad (5)$$

The c.m. energy and the γ -ray energies in eqs. (4) and (5) will be functions of position because of Doppler shift and energy loss in the target:

$$\begin{aligned} E_{\text{c.m.}} &= 0.4297 \left[E_x - x \frac{dE}{dx} \right], \\ E_{\gamma_0} &= \gamma(1 - \beta \cos \vartheta)(E_{\text{c.m.}} + Q_0), \\ E_{\gamma_1} &= \gamma(1 - \beta \cos \vartheta)(E_{\text{c.m.}} + Q_1), \\ E_{\gamma_{429}} &= \gamma(1 - \beta \cos \vartheta)(429.2 \text{ keV}), \end{aligned}$$

where E_x is the incoming beam energy, γ and β are the usual relativistic parameters for the recoiling ${}^7\text{Be}$ nucleus, Q_0 and Q_1 are the Q -values for the ground-state and first-excited-state radiative captures, and ϑ is the γ -ray emission angle measured relative to the beam direction. The energy loss, dE/dx , was calculated from the target density using the formulation of Ziegler¹⁰ for helium ions in helium gas. Similarly, the energy centroid (E_0) of the γ_0 full-energy peak can be written as

$$E_0 = \frac{1}{I_0} \int \frac{E_{\gamma_0}}{E_{\text{c.m.}}} \exp \left[\frac{-164.125}{E_{\text{c.m.}}(\text{keV})} \right] f_0(E_{\text{c.m.}}, \vartheta) \varepsilon(E_{\gamma_0}, x) dx, \quad (7)$$

where I_0 is the integral in eq. (5).

The current (I_c in μA) from the calorimeter controller is equal to the temperature difference ($T_2 - T_1$ in K) between the beamstop and the water-cooled heat sink, and is therefore proportional to the beam power delivered to the calorimeter. Since the beam power is also given by the particle energy times the beam flux in particles per second, we can write

$$E_c \frac{dN_x}{dt} = C(T_2 - T_1), \quad (8)$$

where E_c is the energy of the beam α -particles at the calorimeter (calculated from the observed γ -ray energies and the additional beam-energy loss in the target cell),

and dN_x/dt is the beam particle flux. The number of beam particles is then found by integrating eq. (8):

$$N_x = (C/E_c) \int (T_2 - T_1) dt = (C/E_c) \int I_c dt. \quad (9)$$

The calorimeter current was integrated using a standard beam-current integrator. With no gas in the target, the calibration constant for the calorimeter was measured⁹⁾ to be $C = 1.062 \pm 0.009$ W/K; an additional calculated correction, 0.065 W/K, was added to this constant to take into account the relatively high thermal conductivity of helium.

The gas-target density was calculated from the pressure and temperature of the gas, both of which were assumed to be constant over the length of the target cell (not including the entrance canal). The pressure of the gas was measured with an aneroid pressure gauge, which was calibrated against a McLeod compound manometer. The local gas temperature cannot be measured directly at the beam position, since a radial temperature gradient exists in the target cell, but an upper limit for the temperature of the gas along the beam path can be calculated by assuming that all of the energy deposited in the target is conducted by the gas to the walls of the chamber, which act as an infinite, room-temperature heat sink. This assumption is reasonable because the energy deposited in the extended target was always less than 0.1 W/cm. The temperature difference (T') between two concentric cylindrical surfaces with a heat flow of H W/cm was calculated from the expression

$$T' = (H/2\pi K) \ln(b/a), \quad (10)$$

where K is the thermal conductivity of the gas, b is the inner radius of the target chamber and a is the radius of the beam. This quantity, typically 10 K, was calculated for each run and added to the room temperature to give the target temperature, T . The target number density in atoms per cm^3 is then given by

$$n_t = 9.66 \times 10^{18} p/T, \quad (11)$$

where T is in K and p is in Torr.

The theoretical angular distribution functions of Tombrello and Parker¹¹⁾ were used in the integration of eq. (5). Since only the P_0 and P_2 components have any significant value over the range of energies examined in this experiment, all other components were ignored; thus

$$f_i(E_{c.m.}, \vartheta) = 1 + a_2(E_{c.m.})P_2(\cos \vartheta). \quad (12)$$

Since the theoretical P_2 coefficient is a slowly varying function of energy, it was assumed to be a constant for each of the measurements.

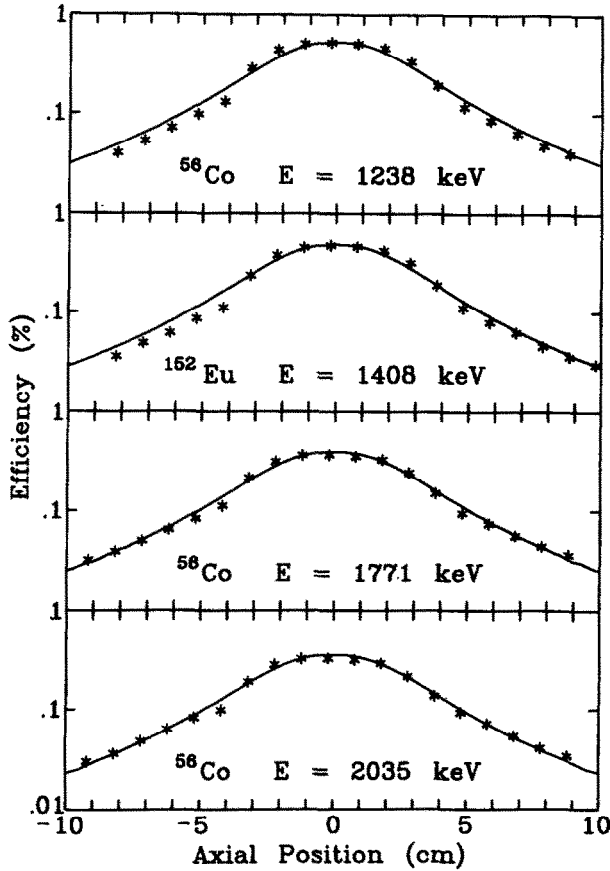


Fig. 7. γ -ray detection efficiencies for the windowless target at several energies as a function of position along the beam axis. Position is measured from the axis of Ge(Li) detector ($x = 0$). The solid curves represent the empirical function used to calculate the experimental cross sections.

For the capture γ -rays, the calibrated-source efficiency data were fitted to an empirical function of the form

$$\varepsilon(E_\gamma, x) = a(E_\gamma)^b / \{1 + [x/(cE_\gamma^d)]^f\}. \quad (13)$$

Fig. 7 shows the measured efficiency as a function of position for several energies corresponding to γ -ray lines from the calibrated ${}^{56}\text{Co}$ and ${}^{152}\text{Eu}$ sources. Also shown in fig. 7 is the best fit of eq. (13) to the data. Since the Doppler broadening of γ_{429} is very small and its γ -ray energy is independent of beam-energy loss in the target, no energy dependence was included in the efficiency function for this transition.

Eqs. (5) and (7) were evaluated numerically to determine $S_i(E)$ for each of the

transitions. The branching ratio is then given by,

$$\rho_i(E_i) = Y_i I_0 / Y_0 I_i, \quad \text{for } i = 1 \text{ and } 429. \quad (14)$$

The total cross-section factor for the ${}^3\text{He}(\alpha, \gamma){}^7\text{Be}$ reaction is equal to the sum of the cross-section factors for radiative capture to the ground state (S_0) and first excited state (S_1) of ${}^7\text{Be}$, where S_1 was taken to be the weighted average of the values calculated from the yields of the two cascade γ -rays, γ_1 and γ_{429} . Similarly, the branching ratio was taken to be the weighted average of ρ_1 and ρ_{429} . The cross sections for the first-excited-state capture branch calculated from the yields of these two γ -rays agreed within the calculated statistical uncertainties.

3.2. GAS-CELL ACTIVITY MEASUREMENTS

In the gas-cell activity measurements the net rate of production of ${}^7\text{Be}$ atoms is given by

$$\frac{dN_{\text{Be}}}{dt} = \int \sigma_{\text{tot}}(E_{\text{c.m.}}) I_x n_t dx - \lambda N_{\text{Be}}, \quad (15)$$

where I_x is the beam current in particles per second, n_t is the target number density and $E_{\text{c.m.}}$ is a function of position because of the energy loss in the target gas,

$$E_{\text{c.m.}}(x) = 0.4297 E_\alpha - \Delta E_{\text{foil}} - x \left. \frac{dE}{dx} \right|_{\text{He}}, \quad (16)$$

where ΔE_{foil} is the average beam-energy loss in the entrance foil.

At the beam energies used in these activity measurements, $\sigma(E_{\text{c.m.}})$ is very nearly linear over the range of energies in the target, and is constant to within 6%. Therefore the integral in eq. (15) can be approximated by a constant production rate,

$$P = \int \sigma(E) n_t I_x dx = \sigma_{\text{tot}}(E_{\text{c.m.}}) N_t I_x, \quad (17)$$

where $E_{\text{c.m.}}$ is the center-of-mass energy at the center of the target and N_t is the total gas-target thickness (in cm^{-2}). At the end of a time period of duration t , with constant beam current and target density, the number of ${}^7\text{Be}$ atoms present will be

$$N_{\text{Be}} = (P/\lambda)(1 - e^{-\lambda t}). \quad (18)$$

In order to take into account the fact that the beam current and target density did not remain exactly constant during bombardment, each production run was

divided into one-hour subperiods and the production was calculated for each subperiod using eq. (17). The resulting ^7Be yields were then multiplied by $\exp(-\lambda\Delta t_i)$ to take into account the decay during the time (Δt_i) between the end of the production subperiod and the beginning of the counting period. The number of ^7Be nuclei at the beginning of the counting period is then given by

$$N_{\text{Be}} = (\sigma_{\text{tot}}/\lambda) \sum_i \{(N_i I_\alpha)_i (1 - \exp(-\lambda t_i)) \exp(-\lambda \Delta t_i)\}, \quad (19)$$

where t_i is the length of the i th production subperiod.

The number of ^7Be decays (Δ_{Be}) during the counting period (Δt_c) is related to the yield of decay γ -rays (Y_{478}) and the number of ^7Be atoms in the catcher foil (N_{Be}),

$$\Delta_{\text{Be}} = Y_{478}/0.104\varepsilon = N_{\text{Be}}(1 - \exp(-\lambda\Delta t_c)), \quad (20)$$

where ε is the detector efficiency and 0.104 is the decay branch to the first excited state of ^7Li . It follows that

$$\sigma_{\text{tot}} = \frac{\lambda Y_{478}}{0.104\varepsilon \sum_i \{(N_i I_\alpha)_i (1 - \exp(-\lambda t_i)) \exp(-\lambda \Delta t_i) (1 - \exp(-\lambda \Delta t_c))\}}. \quad (21)$$

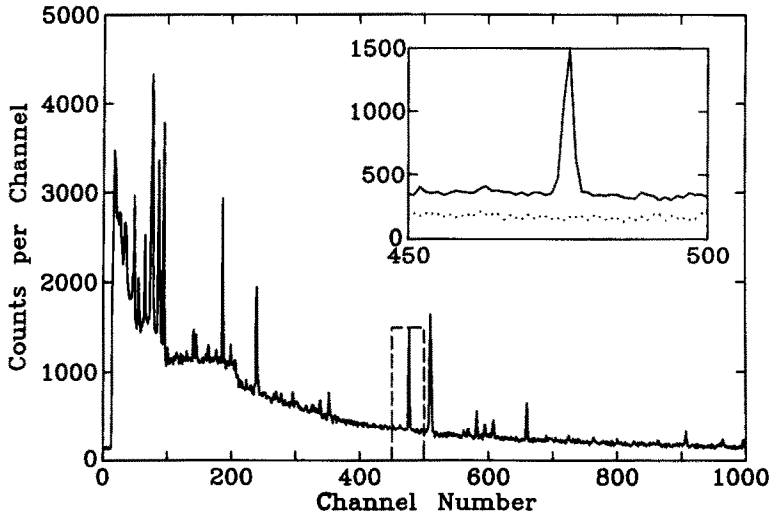


Fig. 8. The γ -ray spectrum from the 144 h count of the platinum catcher foil used in the activity measurement at $E_{\text{c.m.}} = 1255$ keV. The inset shows the γ_{478} peak. The data shown as dots in the inset represent a 72 h count of the entrance foil and the side foil. The total number of counts from the catcher foil is 2227 ± 86 . The number of counts in the side and entrance foil spectrum, using the same peak definition, is 27 ± 40 , consistent with zero.

The catcher-foil γ -ray spectrum for the activation measurement at $E_\alpha = 3400$ keV is shown in fig. 8. The yield of the 478 keV γ -ray was calculated by assuming a linear background as described in subsect. 3.1.

The efficiency was determined by counting with a calibrated ${}^7\text{Be}$ source in the same geometry as the catcher foil. The calibration of this source was based on 1274 keV \times 511 keV coincidence measurements using a ${}^{22}\text{Na}$ source. The target density, n_t , was determined from the pressure and temperature of the gas target where the effective temperature of the target was calculated from the current-dependent shift in the energy of the ${}^{24}\text{Mg}(\alpha, \gamma)$ resonance as described in subsect. 2.2. The observed decrease in effective target thickness was $(6 \pm 2)\%$ at the resonance energy with a beam current of 0.45 ± 0.03 μA , and decreased linearly for currents of 0.30 μA and 0.15 μA . At $E_\alpha = 3400$ keV, the average current was 0.45 μA , corresponding to an effective temperature of 316 ± 6 K; for the $E_\alpha = 2750$ keV measurement, the average beam current was lower but the energy loss was 10% higher, resulting in an effective temperature of 313 ± 6 K.

4. Results

The cross sections and branching ratios extracted for the ${}^3\text{He}(\alpha, \gamma){}^7\text{Be}$ reaction are presented in table 1 and fig. 9. Fits of the theoretical curves of refs. ¹¹⁻¹³)

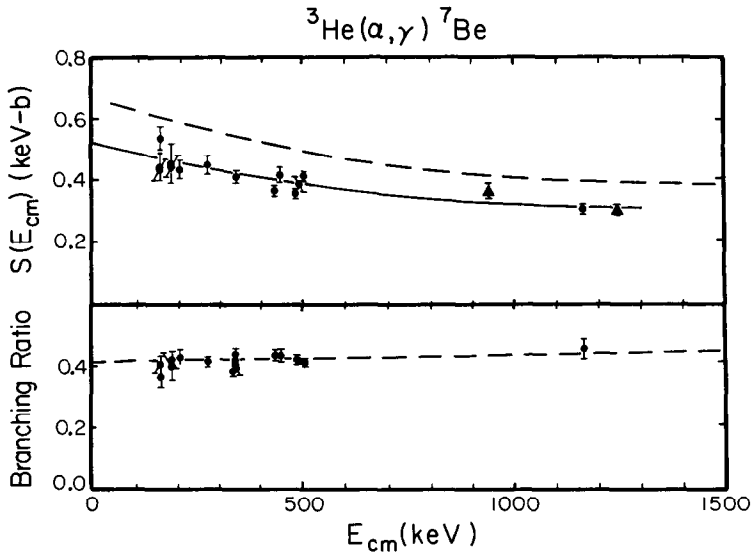


Fig. 9. Summary of the results of the current measurements. The solid curve represents the best fit of the Tombrello and Parker¹¹⁾ calculation to the experimental data. The dashed curve is the unnormalized resonating group calculation of Liu, Kanada and Tang¹³⁾.

TABLE 1

Experimental results for the total cross section, cross-section factors, and branching ratio

(keV)	γ -ray yields			S_0 (keV·b)	S_1 (keV·b)	S_{34} (keV·b)	σ_{tot} (nb)	ρ σ_1/σ_0
	Y_0	Y_1	Y_{429}					
166.6(13)	826	393	632	0.393(29)	0.144(11)	0.536(38)	7.70	0.365(31)
346.6(9)	2719	1245	2644	0.294(16)	0.116(5)	0.410(20)	175	0.394(15)
212.7(13)	1196	611	1154	0.324(18)	0.139(7)	0.463(23)	28.2	0.428(24)
343.6(8)	2424	1167	2409	0.311(16)	0.127(5)	0.438(20)	182	0.408(16)
279.5(8)	2244	1147	2126	0.339(16)	0.140(6)	0.479(20)	93.6	0.414(16)
450.9(13)	1317	713	1409	0.309(13)	0.134(5)	0.443(14)	432	0.434(16)
192.4(22)	389	178	367	0.308(44)	0.123(21)	0.431(60)	16.2	0.399(44)
193.5(12)	996	490	948	0.295(17)	0.124(7)	0.419(20)	16.3	0.421(25)
342.9(9)	2697	1409	2831	0.271(10)	0.119(4)	0.390(11)	161	0.439(16)
343.7(12)	1539	766	1588	0.323(13)	0.137(4)	0.460(14)	192	0.425(19)
496.1(12)	2398	1095	2659	0.277(11)	0.115(5)	0.392(12)	497	0.414(16)
342.6(12)	1346	699	1414	0.292(16)	0.125(6)	0.417(20)	171	0.417(20)
165.5(21)	245	93	160	0.334(38)	0.101(15)	0.435(46)	7.57	0.304(46)
165.8(12)	965	467	869	0.303(19)	0.123(8)	0.426(23)	7.49	0.406(27)
336.7(9)	2468	1067	2321	0.292(11)	0.112(4)	0.404(12)	156	0.404(12)
486.1(11)	3304	1570	3652	0.247(9)	0.104(4)	0.351(10)	421	0.420(15)
437.0(12)	2182	1133	2375	0.250(9)	0.109(4)	0.359(10)	320	0.435(17)
507.4(8)	6651	3173	7210	0.291(9)	0.120(3)	0.411(11)	554	0.411(12)
1169(5)	1091	512	1703	0.210(11)	0.095(5)	0.305(14)	2150	0.454(32)
1255(4)						0.304(16)	2340	
947(5)						0.364(24)	1850	

to the current experimental data measured with the differentially pumped gas target give zero-energy cross-section-factor intercepts of $S_{34}(0) = 0.520$, 0.517 and 0.521 keV·b, respectively. Including the systematic uncertainties in calorimeter calibration, target pressure and detector efficiency, the best experimental S -factor value from the current data is $S_{34}(0) = 0.52 \pm 0.03$ keV·b. Similar theoretical extrapolation for the two gas-cell activity measurements at $E_{\text{c.m.}} = 947$ and 1255 keV yields S -factor intercepts of $S_{34}(0) = 0.55 \pm 0.05$ and 0.52 ± 0.05 keV·b, respectively; the errors in these quantities include systematic errors in the measurement of target pressure, detector efficiency and current integration as well as the uncertainty introduced by variations in the shapes of the various theoretical curves used for the extrapolation.

The results of these two *independent* experiments are in good agreement; a weighted average of the two results gives $S_{34}(0) = 0.53 \pm 0.03$ keV·b. This

agreement depends on the value used for the β -decay branch to the first excited state in ${}^7\text{Li}$. A recently reported measurement of $(15.4 \pm 0.8)\%$ for this branch¹⁴⁾ (versus 10.4% used in this work) would lower the values from the activity measurement by 32% . However, ten more recent measurements of this important branching ratio, using a variety of experimental techniques including that used in ref.¹⁴⁾ have been unable to reproduce this result [see ref.¹⁵⁾ for a list of experiments and measured branches] and, in fact, produce a weighted average of $(10.45 \pm 0.04)\%$, confirming the accepted value.

5. Discussion and conclusions

The cross-section factors, $S_{34}(0)$, measured in the present experiments are in good agreement with the previous prompt γ -ray measurements of Parker and Kavanagh⁵⁾ [$0.47 \pm 0.05 \text{ keV} \cdot \text{b}$], and of Nagatani, Dwarakanath and Ashery^{3,6)} [$0.58 \pm 0.07 \text{ keV} \cdot \text{b}$], and with the more recent ${}^7\text{Be}$ activation measurements of Volk *et al.*¹⁶⁾ [$0.56 \pm 0.03 \text{ keV} \cdot \text{b}$]. The recent activation measurement of Robertson *et al.*¹⁷⁾ is somewhat higher [$0.63 \pm 0.04 \text{ keV} \cdot \text{b}$]. However, all of these results are in serious disagreement with the recently published result of Kräwinkel *et al.*⁴⁾ [$0.30 \pm 0.03 \text{ keV} \cdot \text{b}$].

We are not able to identify the reason(s) for the discrepancy between our measurements and those of ref.⁴⁾, with certainty. We note, however, that there appears to be a substantial discrepancy between the Ge(Li) detector efficiencies quoted by the two experiments. In the Münster experiment, a single commercially prepared ${}^{152}\text{Eu}$ source was used to calibrate the absolute detector efficiency in the windowless target geometry. (At higher energies, reaction γ -rays from ${}^{14}\text{N}(\text{p}, \gamma)$ and ${}^{18}\text{O}(\text{p}, \gamma)$ were measured and normalized to the ${}^{152}\text{Eu}$ source at $E_\gamma = 1408 \text{ keV}$.) In fig. 5 of ref.⁴⁾, the maximum absolute detection efficiency is plotted as a function of γ -ray energy. With an 80 cm^3 Ge(Li) detector located 24 mm from the center of the beam, their measured efficiency for detection of the 1408 keV transition from the ${}^{152}\text{Eu}$ source is given as $\varepsilon = 0.57\%$. For our prompt γ -ray measurements, the detection efficiency was determined by using commercially prepared ${}^{152}\text{Eu}$ and ${}^7\text{Be}$ sources, as well as a ${}^{56}\text{Co}$ source which was calibrated relative to several other well calibrated γ -ray sources. With a 100 cm^3 Ge(Li) detector at a distance of 25 mm from the beam, our measured efficiency for the 1408 keV γ -ray was only $\varepsilon = 0.46\%$.

Although the comparison of the efficiencies of the two detectors will depend on the relative geometry of the two detector crystals and on the amount of γ -ray absorber between the γ -ray source and the detectors, the apparent difference in absolute efficiencies is large enough to account for most of the disagreement between the two experiments.

The branching ratio (σ_1/σ_0) measured with our windowless target is nearly energy independent in good agreement with the theoretical predictions of

refs. ¹¹⁻¹³). The magnitude and energy dependence of this measured ratio also agree with the measurements of refs. ^{4,5}).

The ${}^3\text{He} + {}^4\text{He}$ reduced widths of the bound states, determined by the fit of the Tombrello and Parker theory to the present data, are $\mathcal{R}_{\frac{1}{2}}^2 = 1.29$ and $\mathcal{R}_{\frac{3}{2}}^2 = 1.33$. These values indicate a strong, nearly equal cluster component in both the ground and first excited states of ${}^7\text{Be}$, consistent with the picture of these states as ${}^3\text{He}$ and ${}^4\text{He}$ clusters in a relative p-state.

For the most recent theoretical calculation of solar-neutrino flux ³) a value of $0.52 \pm 0.15 \text{ keV} \cdot \text{b}$ (3σ error) was adopted for the zero-energy intercept of the ${}^3\text{He}(\alpha, \gamma){}^7\text{Be}$ cross-section factor. This value is consistent with the present measurements. The present measurements will therefore have little effect on the magnitude of the predicted solar-neutrino detection rate and will not resolve the solar-neutrino problem.

The authors wish to thank Professor William A. Fowler for his encouragement and guidance throughout these experiments. This work was supported in part by the National Science Foundation under grant no. PHY79-23638.

References

- 1) R. Davis, Jr., D. S. Harmer and K. C. Hoffman, Phys. Rev. Lett. **20** (1968) 1205
- 2) R. Davis, Jr., Science underground, Los Alamos, 1982, AIP Conf. Proc. 96 (AIP, 1983)
- 3) J. N. Bahcall, W. F. Huebner, S. H. Lubow, P. D. Parker and R. K. Ulrich, Rev. Mod. Phys. **54** (1982) 767
- 4) H. Kr  winkel, H. W. Becker, L. Buchmann, J. G  rres, K. U. Kettner, W. E. Kieser, R. Santo, P. Schmalbrock, H. P. Trautvetter, A. Vlieks, C. Rolfs, J. W. Hammer, R. E. Azuma, and W. S. Rodney, Z. Phys. **A304** (1982) 307
- 5) P. D. Parker and R. W. Kavanagh, Phys. Rev. **131** (1963) 2578
- 6) K. Nagatani, M. R. Dwarakanath and D. Ashery, Nucl. Phys. **A128** (1969) 325
- 7) J. L. Osborne, C. A. Barnes, R. W. Kavanagh, R. M. Kremer, G. J. Mathews, J. L. Zyskind, P. D. Parker and A. J. Howard, Phys. Rev. Lett. **48** (1982) 1664
- 8) M. R. Dwarakanath and H. Winkler, Phys. Rev. **C4** (1971) 1532
- 9) J. L. Osborne and A. J. Howard, Nucl. Instr., submitted
- 10) J. F. Ziegler, Helium: stopping power and range in all elemental matter (Pergamon, New York, 1977)
- 11) T. A. Tombrello and P. D. Parker, Phys. Rev. **131** (1963) 2582
- 12) B. T. Kim, T. Izumoto and K. Nagatani, Phys. Rev. **C23** (1981) 33
- 13) Q. K. K. Liu, H. Kanada and Y. C. Tang, Phys. Rev. **C23** (1981) 645
- 14) H. P. Trautvetter, H. W. Becker, L. Buchmann, J. G  rres, K. U. Kettner, C. Rolfs, P. Schmalbrock and A. Vlieks, Verhandl. DPG **VI** (1983) 1141
- 15) R. T. Skelton and R. W. Kavanagh, Nucl. Phys. **A414** (1984) 141
- 16) H. Volk, H. Kr  winkel, R. Santo and L. Wallek, Z. Phys. **A310** (1983) 91
- 17) R. G. H. Robertson, P. Dyer, T. J. Bowles, R. E. Brown, N. Jarmie, C. J. Maggiore and S. M. Austin, Phys. Rev. **C27** (1983) 11